Acta Mech
DOI 10.1007/s00707-016-1754-7

ORIGINAL PAPER

Atilla Altıntaş · Lars Davidson

Direct numerical simulation analysis of spanwise oscillating Lorentz force in turbulent channel flow at low Reynolds number

Received: 8 February 2016 / Revised: 30 September 2016

Abstract Direct numerical simulations of a turbulent channel flow at low Reynolds number ($Re_\tau = 180$, based on the driving pressure gradient and channel half width) are performed. Some results are also presented for $Re_\tau = 400$. In this work we apply an idealized spanwise Lorentz force near the lower wall of the channel and compare the results for the applied force and no-force cases in both the upper half and the lower half of the channel. We have studied two-point correlations to explain the effect of the Lorentz force on streamwise vortices and streaky structures. Despite the observation of clear stabilization of the streaky structures in the vicinity of the wall, the existence of the streamwise vortices is explained by the well-known turbulence regeneration cycle, which improves the understanding of streaky and streamwise vortex structure formation on turbulence generation. Spanwise oscillating Lorentz force effects on the Rankine vortex structures are investigated. Our results lead us to establish an explanation on the effect of sweep and ejection events on the mean vortex structures in the flow field. A mean vortex structure is defined by the time-averaged location of the local minimum and maximum of the streamwise r.m.s. vorticity. We also depict turbulence production rates for both cases and compared the lower and upper half of the channel.

1 Introduction

Flow control has become increasingly important both in terms of environmental health and economic benefits.[1] One of the methods used to study the flow control in wall-bounded flows is to apply an oscillating Lorentz force. In this method, magnets and electrodes are introduced to obtain the Lorentz force in the desired direction. Flow control using the Lorentz force was put forward for the first time to delay the transition of a laminar boundary layer by Gailitis and Lielausis [14]. An experimental study was later performed by Henoch and Stace [17] in which the polarity of the electrodes was arranged to direct the electromagnetic (EM) body force axially downstream and axially upstream. In these experiments a turbulence suppression up to 30% was achieved for the former case with the interaction parameter $St \sim \mathcal{O}(1)$ (St is the ratio of the Lorentz force to the inertial force). However, with the body force axially upstream these researchers found an augmentation of the turbulence. In a numerical study a channel geometry was investigated by Crawford and Karniadakis [9] with the bottom wall subject to streamwise Lorentz forcing in the same way as in Henoch and Stace [17] and they found a similar increase in turbulence.

[1] This paper is an extended version of an accepted talk proceeding paper that appeared as [3].

A. Altıntaş
Engineering Faculty, Karabuk University, 78050 Karabuk, Turkey

L. Davidson (✉)
Division of Fluid Dynamics, Department of Applied Mechanics, Chalmers University of Technology, 412 96 Gothenburg, Sweden
E-mail: lada@chalmers.se

Published online: 03 December 2016

Nosenchuck and Brown [31] designed an array of EM tiles to control the boundary layer which produces a three-dimensional Lorentz force and reported a large amount of drag reduction. However O'Sullivan and Biringen [32] studied a comparable numerical study based on the design of Bandyopadhyay [4] and reported only weak drag reductions. Later on Rossi and Thibault [35] studied similar two-dimensional design of magnets and electrodes and reported similar results with O'Sullivan and Biringen [32]. They both reported that the EM actuator design they used gives strong wall-normal forces, (both wall-ward or opposite depending on the arrangement of magnets and electrodes) outward-directed wall jets, and a vortical structure development above the actuator.

A comprehensive DNS study of a turbulent channel flow performed at different low Reynolds numbers ($Re_\tau = 100, 200, 400$) was presented by Berger et al. [5]. They applied an idealized Lorentz force for both open-loop and closed-loop configurations. In an idealized open-loop case using spanwise forcing, they achieved up to 40% drag reduction. They provided a value of St for the best drag reduction for a given Reynolds number. Du and Karniadakis [11] and Du et al. [12] studied the spanwise traveling Lorentz force, varied continuously both spatially and temporally, where they reported about 30% drag reduction. They noted that in traveling wave excitation, a wide ribbon of low-speed fluid is observed. Breuer et al. [6] applied a similar experiment with Henoch and Stace [17], but the differences in their experiment was the direction of the Lorentz force in spanwise direction. They generated both a uniform spanwise oscillating Lorentz force, similar to Berger et al. [5] simulation, and a spanwise traveling wave. Their results are in good agreement with both Berger et al. [5] and Du et al. [12] results which indicates that drag reduction by Lorentz force is reliable and as predicted by theory.

Beside these studies, an experimental work reported a 47% drag reduction with Lorentz forcing in the spanwise direction by Xu and Choi [38]. Recently Huang et al. [18] applied a spanwise oscillating Lorentz force at the lower wall of a turbulent channel flow and achieved a drag reduction. They noted that a negative spanwise vorticity is generated which makes the streaks tilt and oscillate.

Recently Albrecht et al. [2] performed a numerical study of a flat-plate boundary layer in which a periodic array of flush-mounted, streamwise aligned magnets and electrodes were used. They obtained magnetic induction by using the analytic solution of Akoun and Yonnet [1] and generated a three-dimensional Lorentz force. They made both two-dimensional and three-dimensional studies and reported that two-dimensional calculations using a spanwise-averaged Lorentz force reasonably correspond to three-dimensional simulations.

It is well known that the dominant structures of the near-wall region are the streamwise velocity streaks and the quasi-streamwise vortices [5,21,24,26]. Furthermore, it was shown by Jiménez and Pinelli [21] that a turbulence regeneration cycle exists which does not depend on the outer flow but depends on the local near-wall region. They also proved that the turbulence regeneration cycle depends on two near-wall turbulent structures, the quasi-streamwise vortices, and the streamwise velocity streaks.

There are other explanations of the turbulence generation mechanism in which ring-like vortices are creating strong *sweep* and *ejection* events. Also in these studies vortex structures and streak formations are related. Horseshoe vortices which generate ring-like vortices are responsible for the appearance of streamwise-elongated streaks [15]. Kim [23] showed that the near-wall streamwise vortices are the single most important turbulent structure when studying drag reduction. This is also supported by the observation that streamwise vortices have been found to be responsible for both *ejection* and *sweep* events of the bursting process [34]. These near-wall vortical structures are associated with local high-skin friction regions [7,27,37] which are created by the inrush of high-speed fluid induced by the streamwise vortices. Thus weakening or modifying the streamwise vortices are general approaches in near-wall turbulent control studies, not only in Lorentz force control studies.

In this study, we shed some light on the modification of the near-wall turbulent structures, especially the streamwise vortices and the streamwise velocity streaks, under the influence of the spanwise oscillating Lorentz force. The results presented in this study is important for better understanding the physics of wall turbulence phenomenon and development of improved models of the turbulent production mechanisms and new ways of controlling the wall turbulence. The DNS simulations are performed for a turbulent channel flow (Reynolds number of 180 and 400) in which Lorentz force excitation is applied along the spanwise direction in order to investigate the potential for drag reduction. We performed a detailed analysis of both instantaneous flow fields and various statistical characteristics for both the applied force and the no-force cases.

The paper is organized as follows. First, the methodology and equations are presented, followed by a brief description of the numerical method. In the following section, the results are presented and discussed, and some concluding remarks are given in the final section.

2 Methodology

2.1 Governing equations

The governing equations for an electrically conducting, magnetically permeable, incompressible Newtonian fluid are

$$\frac{\partial \mathbf{u}}{\partial t} + \mathbf{u} \cdot \nabla \mathbf{u} = \hat{\mathbf{e}}_1 \cdot \tilde{\mathbf{I}} - \frac{1}{\rho}\nabla p + \nu \nabla^2 \mathbf{u} + \frac{1}{\rho}(\mathbf{J} \times \mathbf{B}), \tag{1}$$

$$\nabla \cdot \mathbf{u} = 0, \tag{2}$$

$$\nabla \times \mathbf{E} = -\frac{\partial \mathbf{B}}{\partial t}, \tag{3}$$

$$\nabla \times \mathbf{B} = \mu_0 \mathbf{J}_s, \tag{4}$$

$$\mathbf{J} = \sigma(\mathbf{E} + \mathbf{u} \times \mathbf{B}), \tag{5}$$

$$\nabla \cdot \mathbf{B} = 0, \tag{6}$$

$$\nabla \cdot \mathbf{J} = 0. \tag{7}$$

Here, $\mathbf{u}$, p, ρ, ν, $\mathbf{B}$, $\mathbf{J}$, $\mathbf{J}_s$, $\mathbf{E}$, μ_0 and σ are the velocity vector, the pressure, the fluid density, the kinematic viscosity, the magnetic flux density vector, the current density vector, the electrode source current density vector, the electric field vector, the magnetic permeability, and the electrical conductivity of the fluid, respectively. The first term on the righthand side of Eq. (1) is the driving pressure gradient in the streamwise direction. The first two equations are the Navier–Stokes equations and the remaining five are the Maxwell equations. With the assumption of a low conductivity fluid such as seawater (for seawater $\mu_0 \sim \mathcal{O}(10^{-7})$ and $\sigma \sim 2.5 - 5$ Siemens (Ampere/V m)), neglecting the time variation of the magnetic field, and assuming that the induced magnetic field is small compared to the applied magnetic field, we have a potential function ϕ for the electric field. The governing equation for ϕ is a Laplace equation

$$\nabla^2 \phi = 0 \tag{8}$$

and the governing equation for the magnetic flux density reads

$$\nabla^2 \mathbf{B} = 0. \tag{9}$$

With appropriate boundary conditions and by taking the vector product of the current density and the magnetic flux density, the resulting force distribution acts only in the spanwise direction (see [5] for further details). The resulting force can be estimated as a body force in the Navier–Stokes equations. Thus, the governing equations take the following non-dimensional form:

$$\frac{\partial \mathbf{u}}{\partial t} + \mathbf{u} \cdot \nabla \mathbf{u} = \hat{\mathbf{e}}_1 \cdot \tilde{\mathbf{I}} - \nabla p + \frac{1}{Re_\tau}\nabla^2 \mathbf{u} + St\ (\mathbf{J} \times \mathbf{B}), \tag{10}$$

$$\nabla \cdot \mathbf{u} = 0, \tag{11}$$

where Re_τ is the Reynolds number based on u_τ (friction velocity) and δ (half channel height). The friction velocity, u_τ, is based on the driving pressure gradient. $St = J_0 B_0 \delta/(\rho u_\tau^2)$ is the Stuart number, that represents the relative strength of the Lorentz force with respect to the inertia force, where J_0 and B_0 are the current density and the magnetic flux density values at the wall, respectively.

2.2 Force

The spanwise force oscillates in time and decays exponentially in the wall-normal direction,

$$f_z^+ = St\ \exp\left(-\frac{\pi y^+}{a^+}\right) \sin\left(\frac{2\pi t^+}{T^+}\right). \tag{12}$$

The optimal St value for different Reynolds numbers and T^+ values is given as [5]

$$St_{\text{opt}} = 20\left(\frac{Re_\tau \pi}{T^+}\right). \tag{13}$$

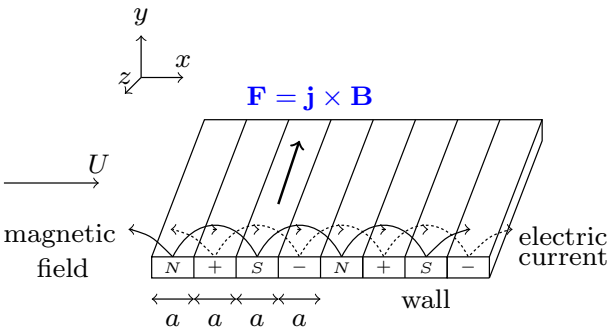

Fig. 1 Arrangement of magnets and electrodes for generating a Lorentz force along the spanwise direction [5]

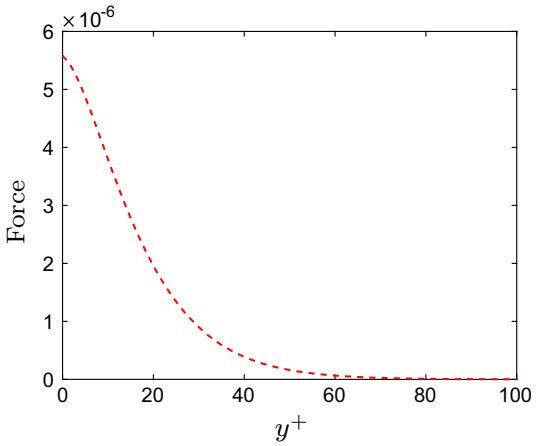

Fig. 2 Force profile

The T^+ parameter is the period of oscillation, and a^+ (the magnet and electrode widths, which here are assumed to be the same) sets the distance the force penetrates into the flow, see Fig. 1; it is here taken as $a^+ = 10\pi$. Lorentz force excitation is applied along the spanwise direction in order to force the flow to oscillate at a certain frequency. We performed simulations for $Re_\tau = 180$ and $Re_\tau = 400$. For $T^+ = 100$, Eq. (13) gives $St = 36\pi$ and 80π for $Re_\tau = 180$ and $Re_\tau = 400$, respectively. We performed simulations not only for these optimal St numbers, but also for $2St_{\text{opt}}$ and $St_{\text{opt}}/2$. The largest drag reductions are obtained with the optimal St number which is in agreement with Berger et al. [5].

The required Lorentz force can be created by placing electrodes and magnets side by side, in the streamwise direction parallel to one another, as shown in Fig. 1. This configuration generates Lorentz force in the spanwise direction, which decays exponentially in the wall-normal direction (Fig. 2). We apply the force in the lower half of the channel, but, because of the exponential function, it decays to zero at $y^+ \simeq 60$.

2.3 Direct numerical simulations

An implicit, two-step time-advancement finite volume methods is used [10]. Central differencing is used in space and the Crank–Nicolson scheme is used in the time domain. When the Navier–Stokes equation (1) for u_i is discretized it can be written as

$$u_i^{n+1} = u_i^n + \Delta t H\left(u_i^n, u_i^{n+1}\right) - \frac{1}{\rho}\alpha\Delta t\frac{\partial p^{n+1}}{\partial x_i} - \frac{1}{\rho}(1-\alpha)\Delta t\frac{\partial p^n}{\partial x_i}, \tag{14}$$

where $H(u_i^n, u_i^{n+1})$ includes convection, the viscous and the source terms, and $\alpha = 0.5$ (Crank–Nicolson). Equation 14 is solved and gives u_i^{n+1}, which does not satisfy continuity. An intermediate velocity field is

computed by subtracting the implicit part of the pressure gradient, i.e.,

$$u_i^* = u_i^{n+1} + \frac{1}{\rho}\alpha\Delta t\frac{\partial p^{n+1}}{\partial x_i}. \tag{15}$$

Taking the divergence of Eq. (15) requiring that continuity (for the face velocities which are obtained by linear interpolation) should be satisfied on level $n+1$, i.e., $\partial u_{i,f}^{n+1}/\partial x_i = 0$, we obtain

$$\frac{\partial^2 p^{n+1}}{\partial x_i \partial x_i} = \frac{\rho}{\Delta t\alpha}\frac{\partial u_{i,f}^*}{\partial x_i}. \tag{16}$$

The numerical procedure at each time step can be summarized as follows [30]:

1. Solve the discretized filtered Navier–Stokes equation for u, v and w.
2. Create an intermediate velocity field u_i^* from Eq. (15).
3. The Poisson equation (16) is solved with an efficient multigrid method [13].
4. Compute the face velocities (which satisfy continuity) from the pressure and the intermediate velocity as

$$u_{i,f}^{n+1} = u_{i,f}^* - \frac{1}{\rho}\alpha\Delta t\left(\frac{\partial p^{n+1}}{\partial x_i}\right)_f. \tag{17}$$

5. Steps 1–4 are performed until convergence (normally two or three iterations) is reached. The convergence for the velocities is 10^{-7} and 10^{-5} for pressure. The residuals are computed using $L1$ norm and they are scaled with the integrated streamwise volume flux (continuity equation) and momentum flux (momentum equations).
6. Next time step.

Note that although no explicit dissipation is added to prevent odd-even decoupling, an implicit dissipation is present. The intermediate velocity field is computed at the *cell centers* (see Eq. (15)) subtracting a pressure gradient. When, after having solved the pressure Poisson equation, the face velocity field is computed, the pressure gradient at the *faces* (see Eq. (17)) is added. This is very similar to the Rhie–Chow dissipation [33].

A constant volumetric driving force is used in the streamwise momentum equation by which the frictional Reynolds number, $Re_\tau = 180$ and 400, is prescribed. Periodic boundary conditions are used in the streamwise and spanwise directions, while the usual no-slip boundary conditions are enforced at the walls. The domain size is $4\pi\delta \times 2\delta \times \pi\delta$ and $2\pi\delta \times 2\delta \times \pi\delta$ with grid sizes $148 \times 98 \times 98$, $98 \times 98 \times 98$, in the streamwise, wall-normal and spanwise directions. The grid resolution is $\Delta x^+ = 15$, $\Delta z^+ = 6$, and $\Delta x^+ = 25$, $\Delta z^+ = 13$, for $Re_\tau = 180$ and 400 case, respectively. A stretching of 1.065 is used in the wall-normal direction. The grid resolution used by Berger et al. [5] was $\Delta x^+ = 20$, $\Delta z^+ = 6.5$ for $Re_\tau = 200$. They tested different box sizes and resolutions for $Re_\tau = 400$, and they reported the same drag reduction trend when they used a grid resolution of $\Delta x^+ = 20$, $\Delta z^+ = 13$.

We employed different box sizes and resolutions for the no-force $Re_\tau = 400$ cases. The box sizes were $1.5\pi\delta \times 2\delta \times 0.5\pi\delta$ and $\pi\delta \times 2\delta \times 0.5\pi\delta$ with grid sizes of $188 \times 98 \times 98$ and $128 \times 98 \times 98$, respectively. Small differences were found in the velocity r.m.s. values (less than 5%).

The non-dimensional time step was kept smaller than $\Delta t^+ = \Delta t u_\tau^2/\nu = 0.6$. The variables u, v, w represent the streamwise, wall-normal, and spanwise velocities, respectively. Before applying any control, all simulations are allowed to reach a fully developed turbulent flow state. The results are, unless otherwise stated, averaged in all homogeneous directions (i.e., x_1, x_3 and t); the average is denoted by an overbar $\overline{(\cdot)}$.

3 Results and discussion

DNS results are presented to analyze the Lorentz force effect. Unless otherwise stated, the results are given for $Re_\tau = 180$ and $Re_\tau = 400$ for optimum St number (36π and 80π, respectively). Figures 3 and 4 present the mean velocity and resolved turbulent fluctuations for applied force and no-force; the latter case is also compared with DNS data [28]. For the no-force case we observe a larger intercept for the log law for $Re_\tau = 180$, compared to the $Re_\tau = 400$ case (Fig. 3) and the u_{rms} profile exhibits a peak at $y^+ = 14$ (Fig. 4), which is in agreement with Moser et al. [28]. They observed that these peak values are larger for higher Re number which is in agreement with our results (Fig. 4).

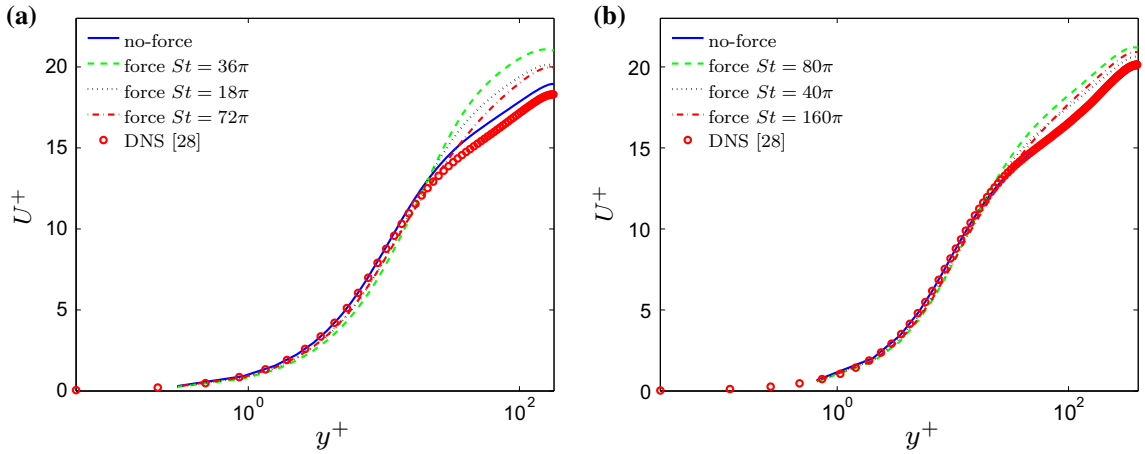

Fig. 3 Mean velocity, U^+ profile. **a** $Re_\tau = 180$, **b** $Re_\tau = 400$

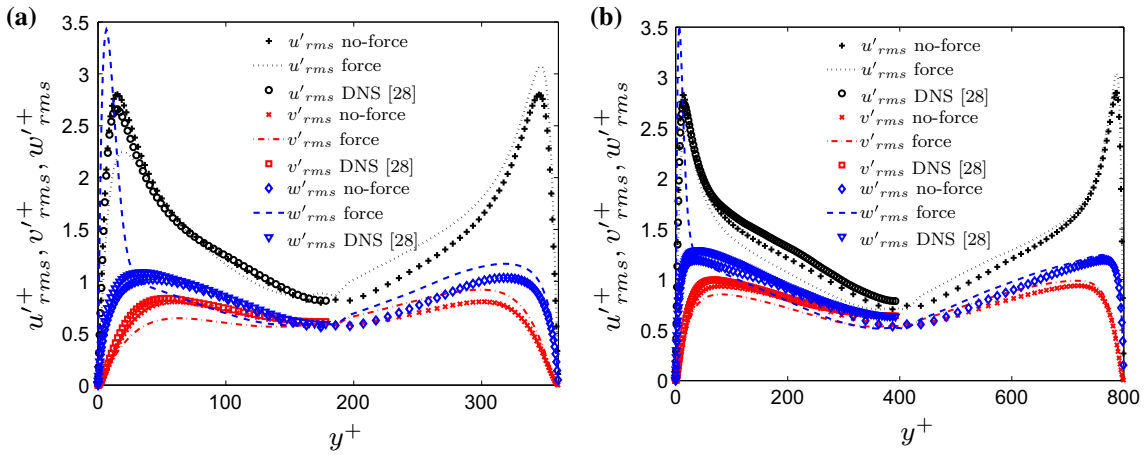

Fig. 4 Root-mean-square velocity fluctuations [3]. **a** $Re_\tau = 180$. $St = 36\pi$, **b** $Re_\tau = 400$. $St = 80\pi$

In Fig. 3, for the applied force case, the viscous sublayer region intercepts with the log-law further away from the wall compared to the no-force case; this is the result of an increased viscous sublayer thickness [8]. In the lower half of the channel smaller u_{rms} and v_{rms} are obtained in the applied force case compared to the no-force case; the spanwise r.m.s. velocity (Fig. 4) exhibits a peak near the lower wall (Fig. 5). Lower Reynolds shear stress compared to the no-force case shows that the Lorentz forcing gives a turbulence drag reduction (Fig. 6). This is also seen by the fact that the bulk velocity increases with forcing by 18% ($St = 36\pi$) compared to the no-force case. Figure 6 clearly shows that $St = 36\pi$ is the frequency which is most efficient in reducing the shear stress (and hence the drag). For the applied force case, we observe a maximum of approximately 40 and 24% drag reduction for $Re_\tau = 180$ and $Re_\tau = 400$ cases, respectively, which is in agreement with the findings of Berger et al. [5]. For both Reynolds numbers, the spanwise r.m.s. velocity peak values coincide for corresponding St numbers (Fig. 5a, b). However, when we compare Fig. 6a, b, while $St_{\text{opt}}/2$ provides the second best reduction for the Reynolds shear stress for $Re_\tau = 180$, it is $2St_{\text{opt}}$ for $Re_\tau = 400$. This result is expected since the second largest mean velocity values are obtained for $St_{\text{opt}}/2$ for the $Re_\tau = 180$ case, while it is $2St_{\text{opt}}$ for the $Re_\tau = 400$ case, see Fig. 3a, b.

Two-point correlations are very effective for understanding the structure of the flow. Pick two points along the x_1 axis, say x_1^A and x_1^C, and sample the fluctuating velocity in the x_1 direction. Then the correlation of the velocity u_1' is given by

$$B_{uu}(\hat{x}_1) = \overline{u_1'(x_1)u_1'(x_1 - \hat{x}_1)}, \tag{18}$$

where $\hat{x}_1 = x_1^A - x_1^C$. Figures 7, 8 and 9 present these correlations in the spanwise direction for both the upper and the lower half of the channel. Since the force is applied only in the lower half of the channel, the two-point

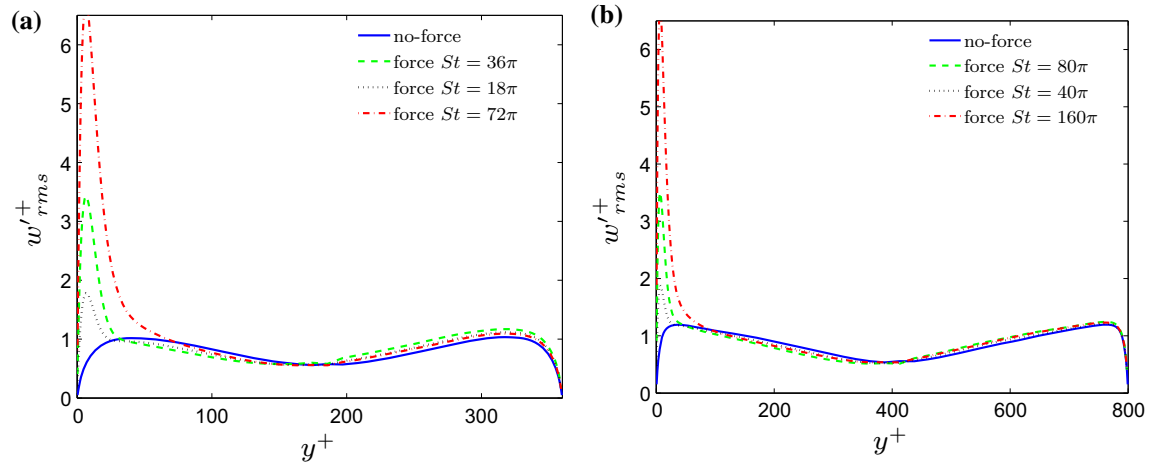

Fig. 5 Spanwise r.m.s. fluctuations. **a** $Re_\tau = 180$, **b** $Re_\tau = 400$

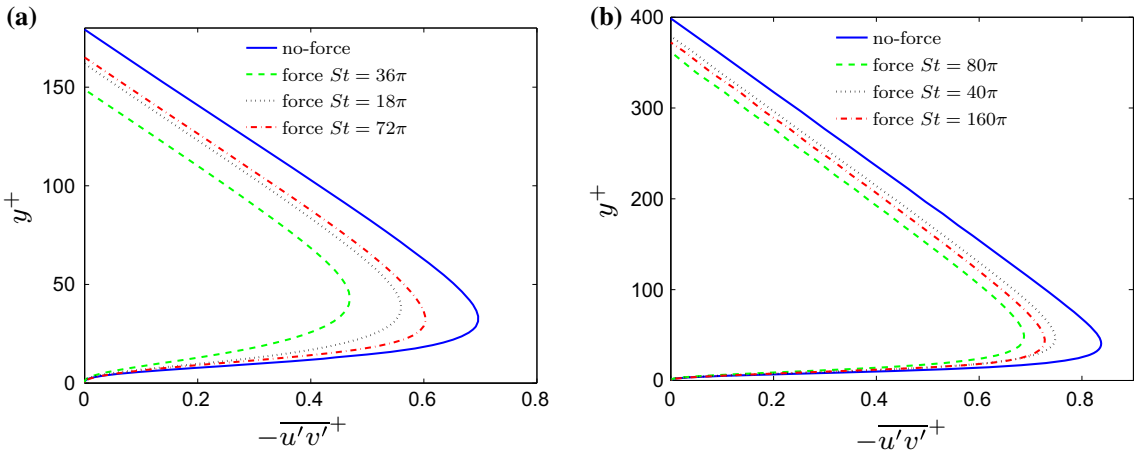

Fig. 6 Reynolds shear stress. **a** $Re_\tau = 180$, **b** $Re_\tau = 400$

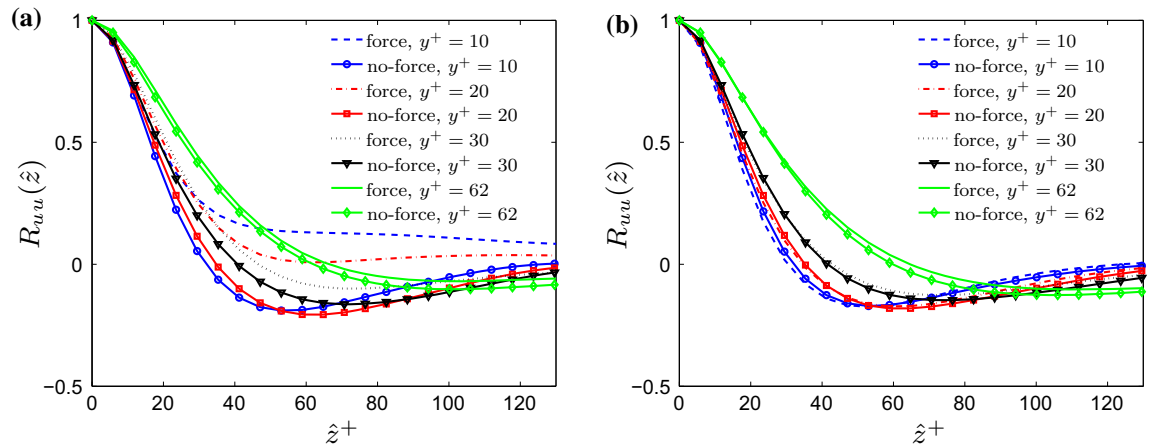

Fig. 7 Streamwise two-point velocity correlations. $Re_\tau = 180$. $St = 36\pi$. **a** Lower wall [3], **b** upper wall

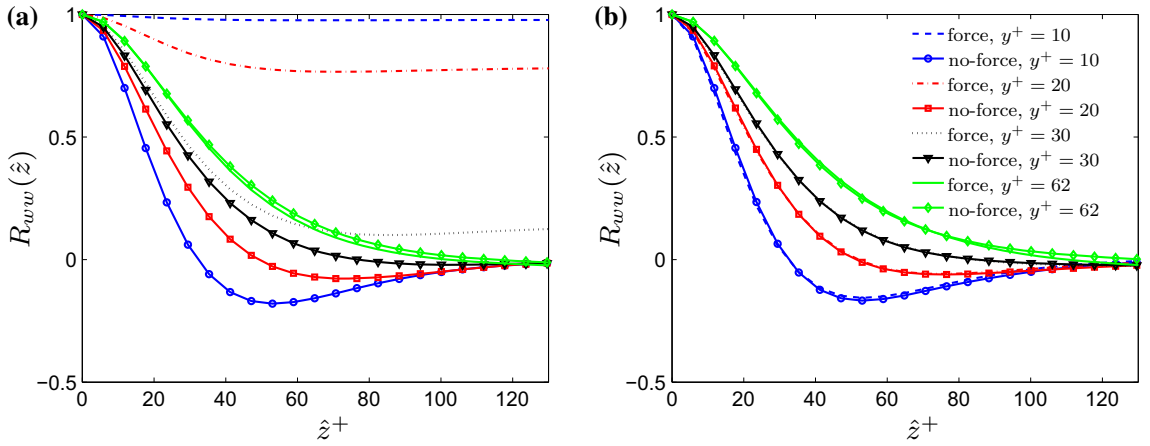

Fig. 8 Spanwise two-point velocity correlations. $Re_\tau = 180$, $St = 36\pi$. (The legend of **b** also apply for the **a**). **a** Lower wall, **b** upper wall

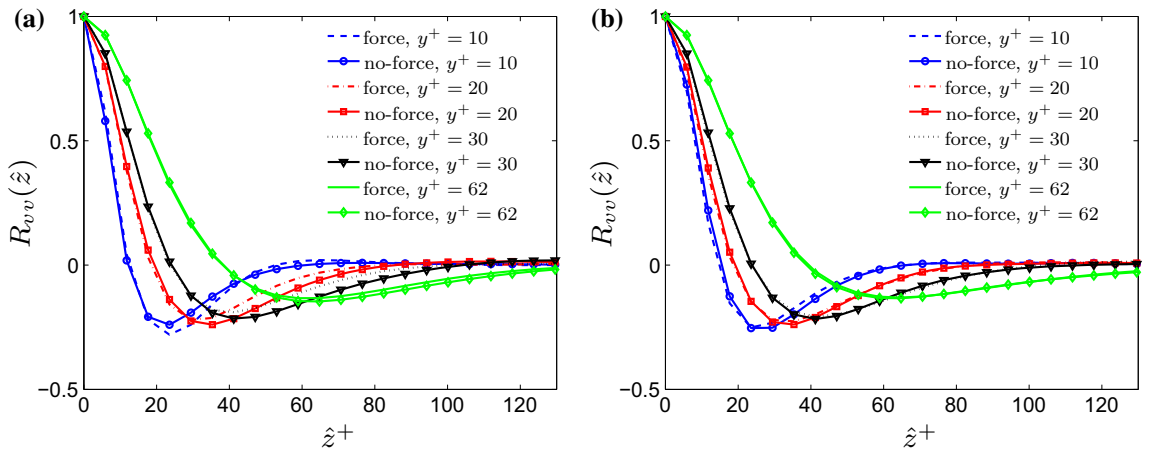

Fig. 9 Wall-normal two-point velocity correlations. $Re_\tau = 180$, $St = 36\pi$. **a** Lower wall, **b** upper wall

correlations in the upper half are very similar for the applied force and the no-force cases (Figs. 7b, 8b, 9b). In the area in which the force is effective, the applied force correlation values are very different from the no-force case for the streamwise and spanwise correlations (Figs. 7a, 8a), except for $y^+ > 62$, where the force is close to zero, see Fig. 2. However, the wall-normal correlations are very similar for both applied force and no-force cases (Fig. 9a). The cause of this result is investigated below.

Streamwise velocity two-point correlation carries information about the mean spacing between the streaks. In Fig. 7a, the no-force correlation values become negative and reach a minimum at approximately $z^+ = 54$ for $y^+ = 10$ and 20, which provides an estimate of the mean separation between the high- and the low-speed fluid; the mean spacing between the streaks of high- and low-speed fluid should be roughly twice that of the mean separation [25].

The regeneration cycle of low-speed streaks and streamwise vortices which is called the "streak cycle" is investigated by Hamilton et al. [16] and Jiménez and Pinelli [21]. In their study they showed that the cycle is governed by the streak instability which generates tilted streamwise vortices. The streamwise vortices in turn assemble low-speed fluid and generates low-speed streaks. These streaks undergo wavy motions, i.e., streak instability occur. For the applied force case, the $R_{uu}(z)$ profiles do not exhibit any minimum for $y^+ = 10$ and only a weak minimum for $y^+ = 20$, which may indicate the absence of streaky structures [8] or more stable or weak streaky structures compared to the no-force case [21]. The absence of a minimum may also indicate an enlargement of the streaks in the spanwise direction [8,29]. This means that, however, the change in the $R_{uu}(z)$ profiles show that forcing modifies the wall streaks, we have not yet sufficient information to determine

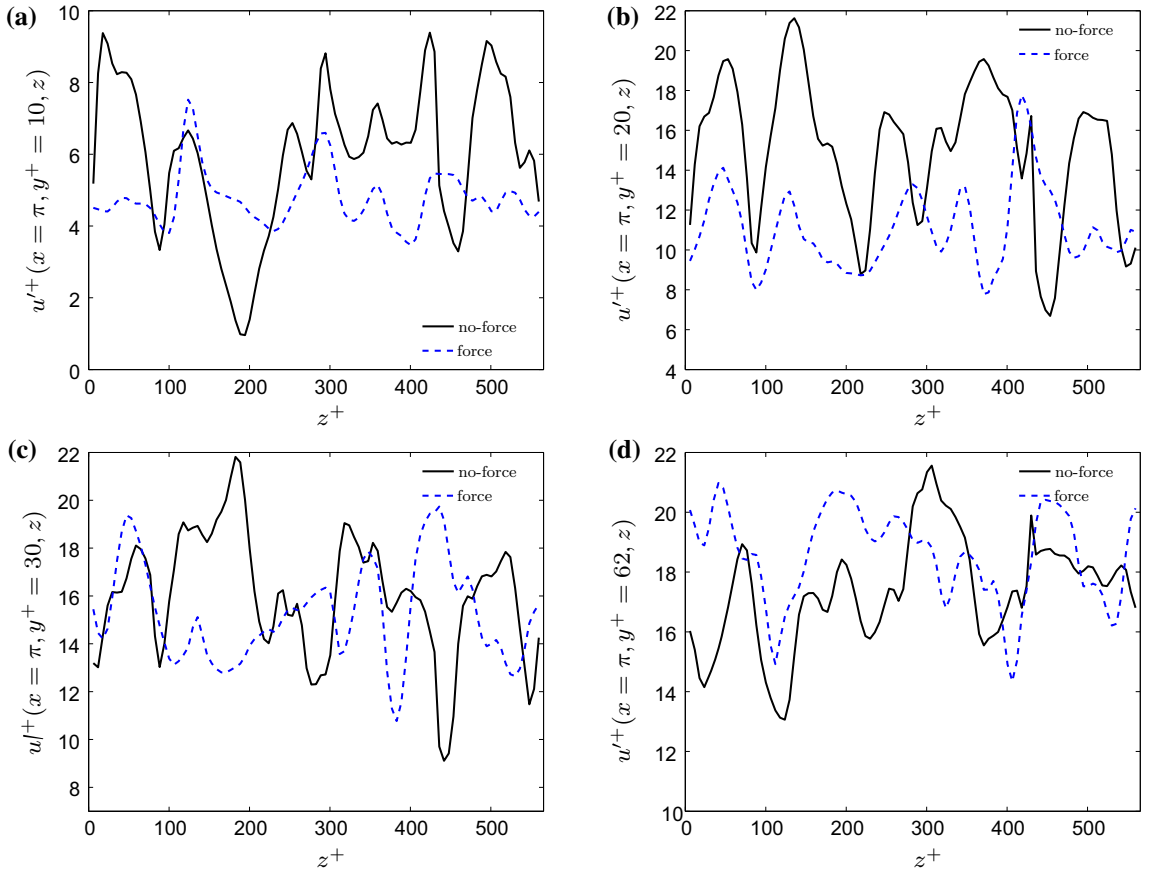

Fig. 10 Streamwise fluctuation velocity computed with Eq. (19). $x = \pi$. $Re_\tau = 180$, $St = 36\pi$. **a** $y^+ = 10$, **b** $y^+ = 20$, **c** $y^+ = 30$, **d** $y^+ = 62$

the way in which this modification occurs. The discussion below gives further insight into modification of the streaky structures.

The presence of a minimum in the $R_{ww}(z)$ profiles (Fig. 8) was originally believed to be related to the separation of two streamwise vortices [29]. Later on, the cause of this minimum in $R_{ww}(z)$ was found to be impingement of high-speed fluid at the wall (splatting) [22,25]. Figure 10a, b, which are generated by Eq. (19), show that the oscillating Lorentz force gives a smoother streamwise velocity in the spanwise direction near the wall, which can also be seen in the plots of the r.m.s. streamwise velocity fluctuations, see Fig. 4 (this figure also shows that the wall-normal r.m.s. velocity fluctuations are smaller in the applied force case). Hence, the lower u_{rms} and v_{rms} in the applied force case compared to the no-force case may explain why the splattings are not visible in the former case (Fig. 8a).

The presence of the minimum in the $R_{vv}(z)$ profiles is consistent with the existence of streamwise vortical structures in the wall region [25] (a mean vortex structure is defined by the time-averaged location of the local minimum and maximum of the streamwise r.m.s. vorticity). The minimum in $R_{vv}(z)$ is related to the mean spanwise distance across a vortex. The larger separation in the z-direction for increasing wall distance indicates larger diameters of the vortices away from the wall [29]. The $R_{vv}(z)$ values are very similar for the applied force and the no-force cases (Fig. 9a), which suggests that the spanwise oscillating Lorentz force does not affect the mean distance between the streamwise vortices.

To better understand the force effect on the streaky structures, we investigated the streamwise fluctuation velocities in the spanwise direction for different y^+ values (Eq. (19)),

$$u'(x, y, z, t) = u(x, y, z, t) - \bar{u}(y). \tag{19}$$

The results are given in Fig. 10, where the applied force and the no-force cases are compared. It is clearly seen that, for $y^+ = 10$ and $y^+ = 20$, the streamwise fluctuating velocity is smaller in the applied force case, which

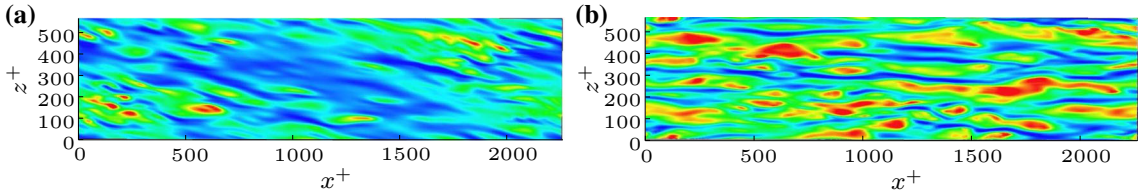

Fig. 11 Streamwise velocity (u) contours for the same instant for lower and upper wall, $y^+ = 10$. $Re_\tau = 180$, $St = 36\pi$. Applied force case. *Blue color* indicates low-speed streaks, *yellow-red* high-speed streaks. **a** Lower wall, **b** upper wall (color figure online)

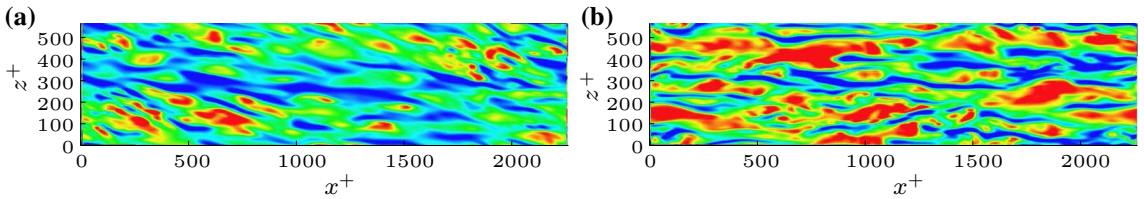

Fig. 12 Streamwise velocity (u) contours for the same instant for lower and upper wall, $y^+ = 20$. $Re_\tau = 180$, $St = 36\pi$. Applied force case. *Blue color* indicates low-speed streaks, *yellow-red* high-speed streaks. **a** Lower wall, **b** upper wall (color figure online)

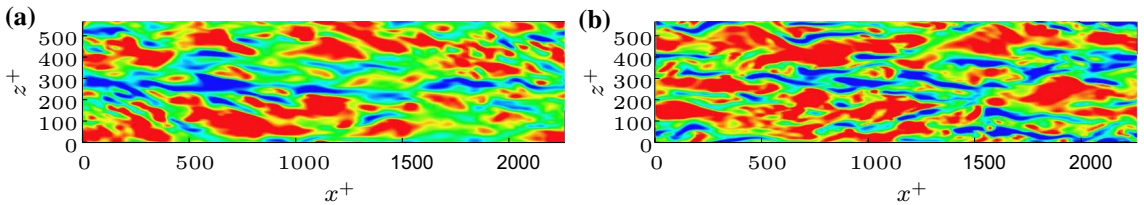

Fig. 13 Streamwise velocity (u) contours for the same instant for lower and upper wall, $y^+ = 30$. $Re_\tau = 180$, $St = 36\pi$. Applied force case. *Blue* indicates low-speed streaks and *yellow-red* high-speed streaks. **a** Lower wall, **b** upper wall (color figure online)

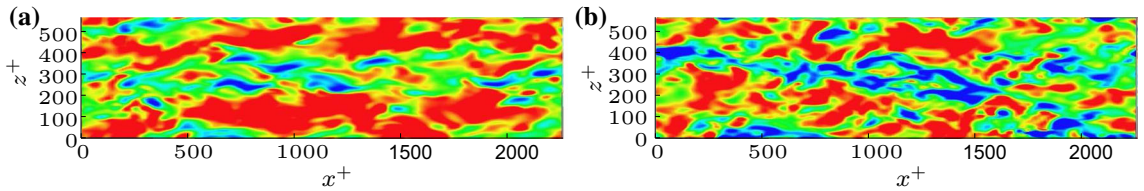

Fig. 14 Streamwise velocity (u) contours for the same instant for lower and upper wall, $y^+ = 62$. $Re_\tau = 180$, $St = 36\pi$. Applied force case. *Blue* indicates low-speed streaks and *yellow-red* high-speed streaks. **a** Lower wall, **b** upper wall (color figure online)

means that although the streaky structures exist at these y^+ levels, they are more stable than in the no-force case.

The streamwise fluctuations vary around $1-9$ for the no-force case compared to around $4-7$ for the applied force case for $y^+ = 10$ (Fig. 10a), while the fluctuation velocity is around $7-22$ and $8-18$ for the no-force and applied force cases, respectively, for $y^+ = 20$ (Fig. 10b). The situation is reversed further away from the wall (Fig. 10c), and for $y^+ = 60$ the high-speed velocity fluctuations in the applied force case are larger than those in the no-force case (Fig. 10d). Figures 11, 12, 13 and 14 present the contour plots of the streamwise velocity, u, at $y^+ = 10,\ 20,\ 30$ and 62 for the applied force case for the upper and lower walls for the same instantaneous flow field. For $y^+ = 10$, it is clear that for the applied force case, the high-velocity streaks near the lower wall, are suppressed and the low-velocity streaks dominate unlike for the upper wall (Figs. 11, 12). There is also an inclination of the wall streaks with respect to the flow direction due to the spanwise flow component for the lower wall. A similar inclination was also observed by Du et al. [12]. Further away from the wall, the high-velocity streaks dominate, the fundamental characteristics of the streaky structures remain the same, and no inclination is observed for $y^+ > 30$ (Figs. 13, 14).

Here arises a question: why is there a clear stabilization of the streaky structures near the wall, but no visible change in the existence of the streamwise vortices (see Fig. 9a)? This question is answered by Jiménez

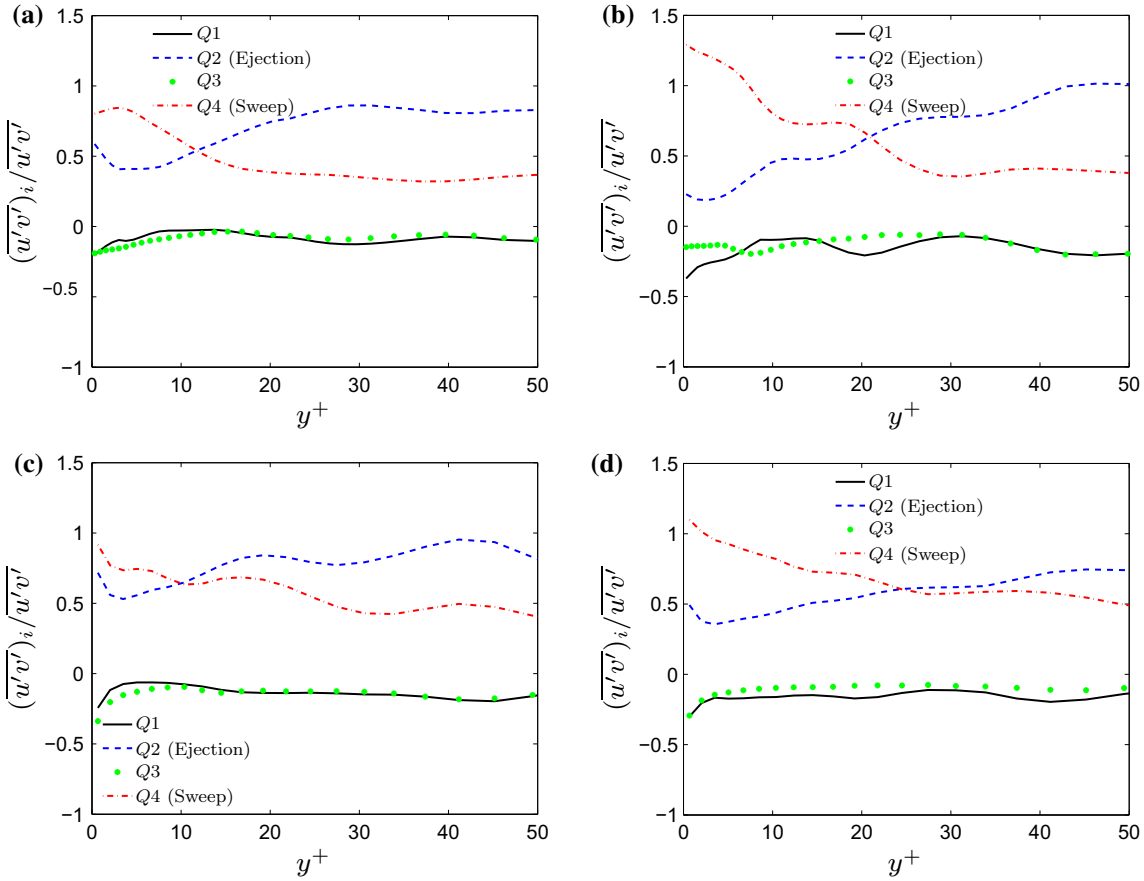

Fig. 15 Reynolds shear stress from each quadrant normalized by the local mean Reynolds shear stress. Subscript i denotes the quadrant number, Q_i. **a** No-force case, $Re_\tau = 180$. $St = 36\pi$, **b** applied force case, $Re_\tau = 180$. $St = 36\pi$, **c** no-force case, $Re_\tau = 400$. $St = 80\pi$, **d** applied force case, $Re_\tau = 400$. $St = 80\pi$

and Pinelli [21]. These authors studied the turbulence production mechanism in the near-wall region. They first proved that the streak cycle is the key regeneration mechanism of turbulence. They damped the streak component of the wall-normal vorticity completely by multiplying it by a filter function near the lower wall, while the upper wall remained unchanged. In this way they laminarized the turbulence at the lower wall. However, the most important experiment they carried out was to define the region in which the instabilities of the streaks give rise to streamwise vortices. Surprisingly, they found that filtering applied for $0 < y^+ < 20$ was not effective, but the flow laminarized completely when the filtering was applied for $y^+ \gtrsim 60$. In short, the regeneration cycle depends on the flow region $20 \leq y^+ \leq 60$.

In our study we find that while the streaks for the applied force case are more stable at $y^+ < 20$, their fundamental structure further away from the wall remains the same as in the no-force case, which means that the streak cycle is hardly affected; streamwise vortices are present in both cases (see Figs. 13, 14).

A quadrant analysis of the Reynolds shear stresses was performed to better compare the flow field structures for the applied force and the no-force cases. To achieve accurate results, 400 data sets were used for each y^+, see Fig. 15. Very similar results are obtained in the no-force case (Fig. 15a) compared with Kim et al. [25], where they also see dominant sweep events up to a level of $y^+ \approx 12$. In the applied force case, the fourth quadrant events (sweep) dominate over second quadrant events (ejection) up to approximately $y^+ = 20$ (Fig. 15b). Similar results are observed for $Re_\tau = 400$ (Fig. 15c, d).

Figure 16 presents the Reynolds shear stress contribution from the second and fourth quadrants, normalized by the wall shear stress. It is obvious that in the applied force case there is a shift of the sweep and ejection events away from the wall which proves that, in the applied force case, the vortex structures are moved away from the wall. As a result of the turbulence suppression, second and fourth quadrant events, which are the cause of turbulence, are lower in the applied force case compared to the no-force case. It is also seen that

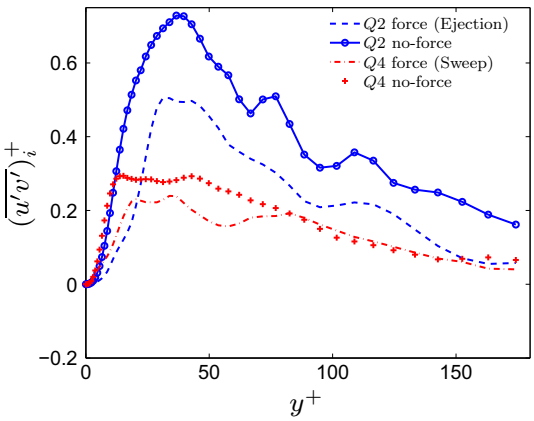

Fig. 16 Quadrant analysis of sweep and ejections. $Re_\tau = 180$, $St = 36\pi$. Subscript i denotes the quadrant number, Q_i

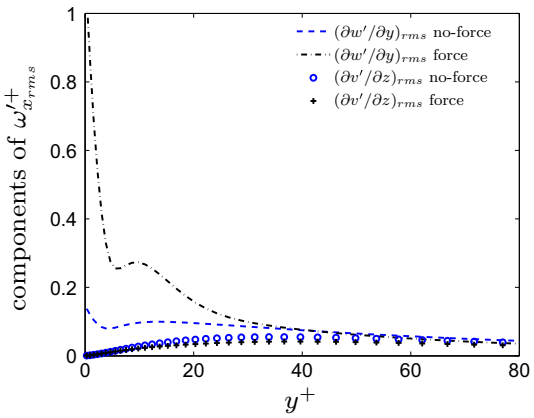

Fig. 17 The two terms of $\omega'_{x_{\text{rms}}}$. $Re_\tau = 180$, $St = 36\pi$

the forcing reduces the ejection events much more than the sweep events. Similar quadrant analysis results were reported in a study in which turbulent flow relaminarization was obtained at a low Reynolds number by reducing the Reynolds number [19]. They also got lower sweep and ejection events compared to the higher Reynolds number, and the sweep events moved away from the wall.

Berger et al. [5] noticed that the key to drag reduction is to perturb the near-wall streamwise vortices, and postulated that an effective way to achieve this goal is to introduce Lorentz force perturbations perpendicular to the axes of the near-wall streamwise vortices. At the very beginning of their study, before determining the optimum parameters for spanwise oscillated Lorentz force, they chose the penetration depth as $a^+ = 10\pi$ which they expected would give the greatest effect on the streamwise vortices based on the mean vortex model defined by Kim et al. [25]. They used the Rankine vortex model of Kim et al. [25] to approximate the effective penetration depth, and they did not further investigate the modification of this model based on the spanwise oscillated Lorentz force. However, defining the modification of the mean streamwise vortices geometrically could be important to improve the existing flow control methods and/or may lead to new control approaches. In order to define the modification of the mean streamwise vortices, we consider the streamwise r.m.s. vorticity which gives information about the streamwise vortex structures; the minimum point of the streamwise r.m.s. vorticity gives the edge of the mean Rankine vortex structure [25,29], and the maximum point gives the center of the mean Rankine vortex [25]. If we consider the two terms, $\partial w'/\partial y$ and $\partial v'/\partial z$ of ω'_x separately, we find that its minimum and maximum locations are defined by $\partial w'/\partial y$, see Fig. 17. In other words, this indicates that the streamwise vorticity defines the radius of the mean Rankine vortex in the wall-normal direction. The forcing gradient, $\mathrm{d}f/\mathrm{d}y$ (see Eq. (12)), gives rise to an increase of $\partial w'/\partial y$, which explains why $\omega'_{x_{\text{rms}}}$ is larger at the wall in the applied force case as compared to the no-force case, see Fig. 18. This figure also shows that the minimum and maximum points in the applied force case are closer to each other than in the no-force case (for the no-force case: $y^+_{\text{min}} \approx 5$, $y^+_{\text{max}} \approx 18$, for the applied force case: $y^+_{\text{min}} \approx 6$, $y^+_{\text{max}} \approx 10$). This means

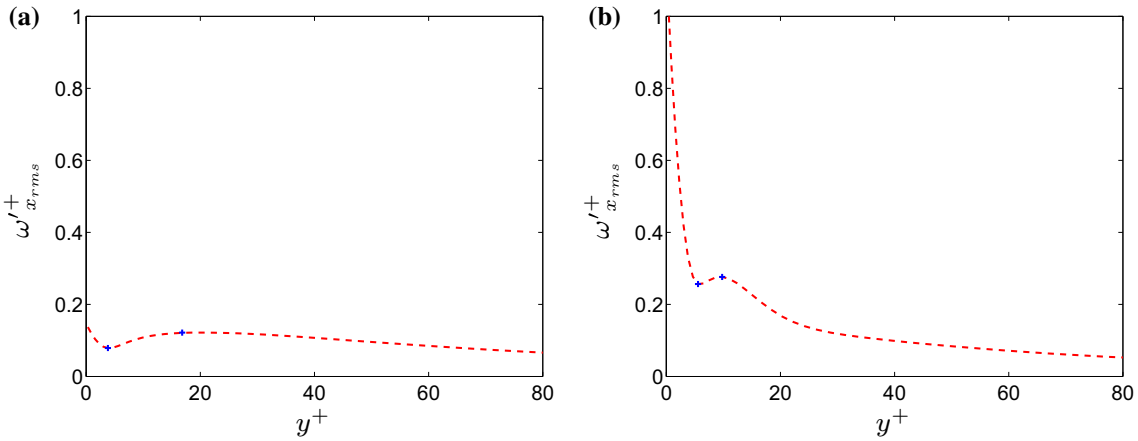

Fig. 18 Root-mean-square streamwise vorticity fluctuations. $Re_\tau = 180$, $St = 36\pi$. +: minimum and maximum of $\omega'^{+}_{x_{\text{rms}}}$. **a** No-force case, **b** applied force case

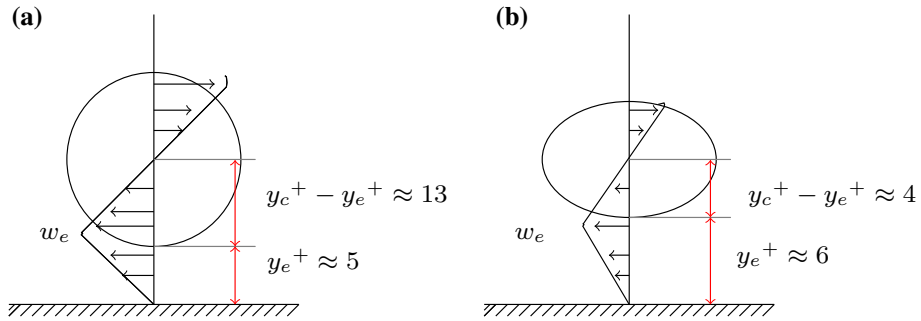

Fig. 19 Mean Rankine vortex illustrations. c and e denote the center and the edge of the vortex, respectively. **a** No-force case, mean Rankine vortex illustration, **b** applied force case, mean Rankine vortex illustration

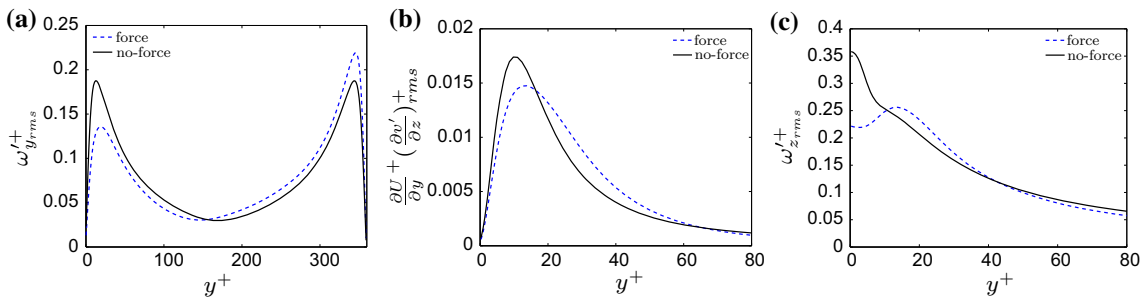

Fig. 20 Wall-normal fluctuation vorticity, $\omega'_{y_{\text{rms}}}$, a $\omega'_{y_{\text{rms}}}$ source term, $\frac{\partial U}{\partial y}^{+}(\frac{\partial v'}{\partial z})^{+}_{\text{rms}}$, and spanwise fluctuation vorticity, $\omega'^{+}_{z_{\text{rms}}}$. $Re_\tau = 400$, $St = 80\pi$. **a** Wall-normal fluctuation vorticity, $\omega'_{y_{\text{rms}}}$, **b** a streamwise vorticity source term, $\frac{\partial U}{\partial y}^{+}(\frac{\partial v'}{\partial z})^{+}_{\text{rms}}$, **c** Spanwise fluctuation vorticity, $\omega'^{+}_{z_{\text{rms}}}$

that we have a smaller radius of the mean streamwise vortex in the wall-normal direction in the applied force case than in the no-force case. However, the $R_{vv}(z)$ profile (see Fig. 9a) suggests that there is no change in the Rankine vortex radius in the spanwise direction. This analysis leads us to suggest that the spanwise Lorentz force modifies the mean Rankine vortex into a shape that is elliptic and has a smaller extent in the wall-normal direction than in the spanwise direction, see Fig. 19.

According to the Schoppa and Hussain [36], the normal vorticity ω'_y is a key indicator of formation of new streamwise vortices near the wall by streak instability. The growth rate of the streaks' sinus instability mode grows with the magnitude of ω'_y , and if it falls below a threshold no such instability occurs. Figure 20a presents $\omega'_{y_{\text{rms}}}$ which shows that the vorticity fluctuations in the applied force case are reduced compared to the no-force

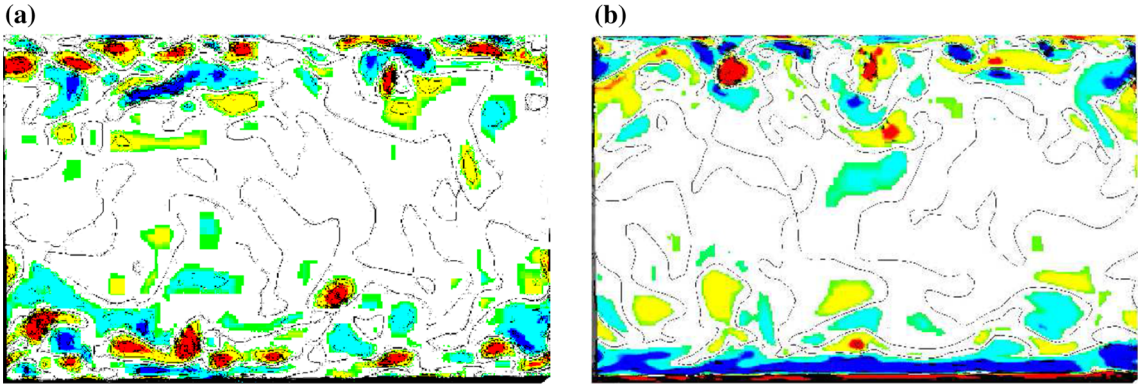

Fig. 21 Streamwise vorticity for applied force and no-force cases. $Re_\tau = 180$, $St = 36\pi$. **a** No-force, **b** force

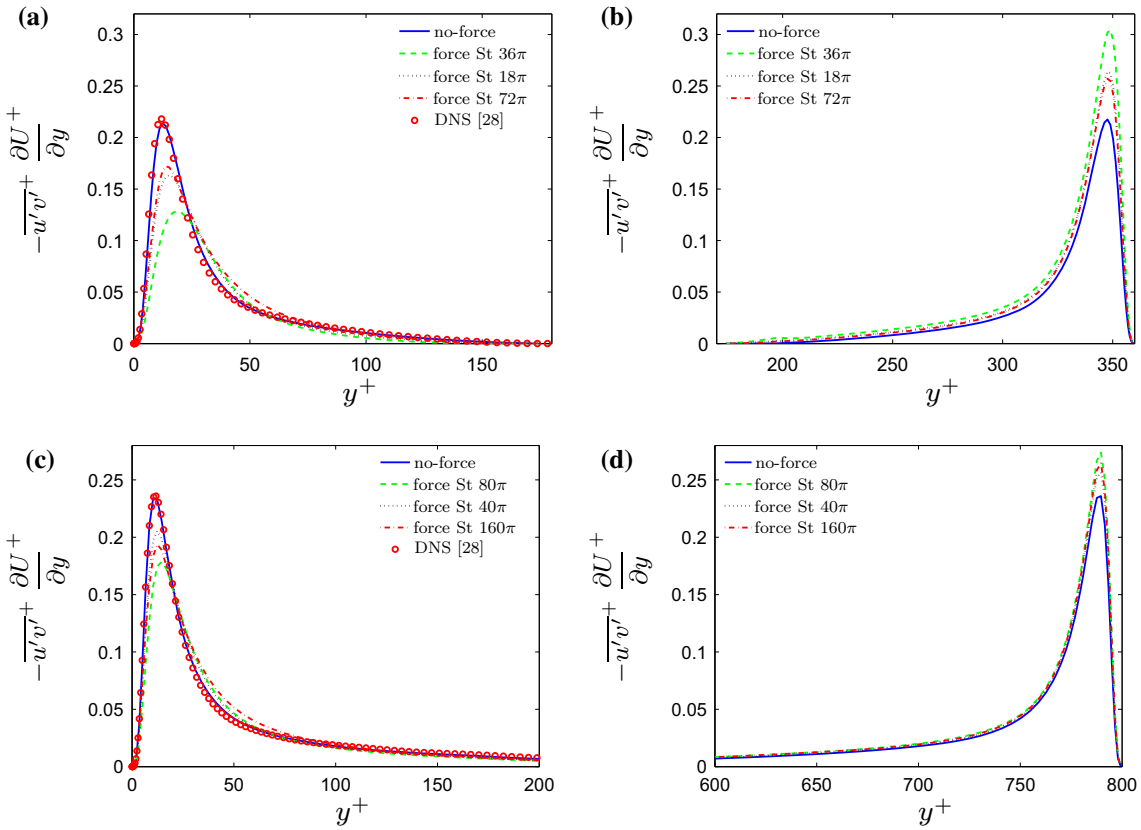

Fig. 22 Turbulence production. **a** Lower wall, $Re_\tau = 180$, **b** upper wall, $Re_\tau = 180$, **c** lower wall, $Re_\tau = 400$, **d** upper wall, $Re_\tau = 400$

case about a factor of 1.4. At the upper wall, $\omega'_{y_{\text{rms}}}$ is a factor of 1.2 smaller in the applied force case. Kim [24] defines the term, $\frac{\partial U}{\partial y}\frac{\partial v'}{\partial z}$, as a source term for wall-normal vorticity and relates it with the regeneration cycle as a first leg of the streak formation mechanism. Figure 20b exhibits lower $\frac{\partial U}{\partial y}(\frac{\partial v'}{\partial z})_{\text{rms}}$ values for the applied force case compared to the no-force case, and the peak is in the former case shifted away from the wall. In addition, Kim [24] pointed out that interaction of wall-normal and spanwise velocities, which is independent of the streamwise direction, with the mean shear, $\frac{\partial U}{\partial y}$, creates streaks. Another significant evidence of the stabilization of the streaky structures for the applied force case compared to the no-force case is the lower spanwise fluctuation vorticity, $\omega'_{z_{\text{rms}}}$, in the vicinity of the applied force wall (Fig. 20c) which indicates the presence of low- and high-speed streaks [20]. We presented u' in Fig. 10 which indicates that the streaky

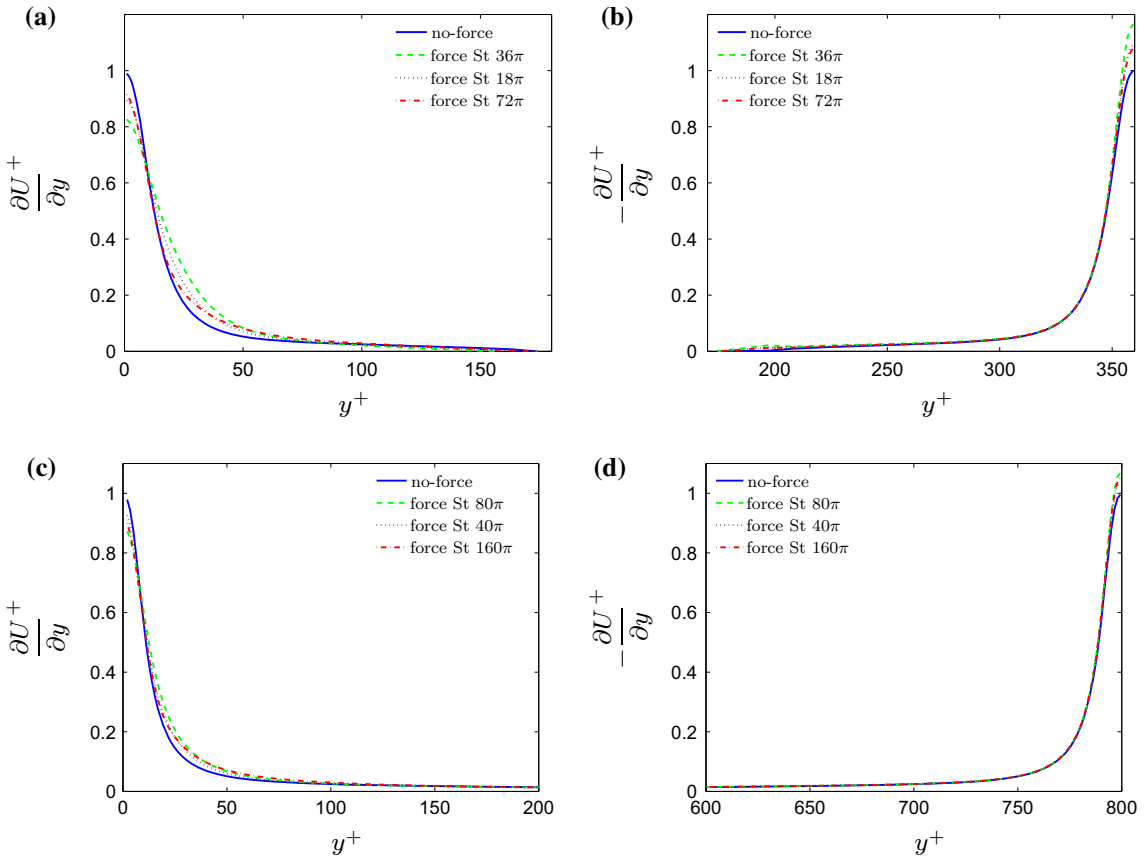

Fig. 23 Mean velocity gradient. **a** Lower wall, $Re_\tau = 180$, **b** upper wall, $Re_\tau = 180$, **c** lower wall, $Re_\tau = 400$, **d** upper wall, $Re_\tau = 400$

structures are more stable in the applied force case in the vicinity of the wall (Fig. 10a, b). The more stable streaky structures are also in agreement with Figs. 11a, 12a and 7a, where it is shown how the streaks are modified in the applied force case. The reduction in the magnitude of $\omega'_{y_{rms}}$ indicates reduced sinus instability in the streaks which reduces formation of new streamwise vortices.

Figure 21b compared to Fig. 21a suggests that in the applied force case the vortex structures near the lower wall are suppressed and/or weakened while the streamwise vorticity increases. This is in agreement with Figs. 18c and 20a which together suggest that while the streamwise vorticity is enhanced the streamwise structures are suppressed or weakened. Note that the streamwise vortices are not completely suppressed, nor are the streaks totally stabilized, otherwise the turbulence regeneration cycle could not be sustained [21]. This is in agreement with Fig. 9a (there is a distinct minimum) which shows that the streamwise vortex structures still exist near the lower wall in the applied force case. A similar figure as Fig. 21 has been reported by Berger et al. [5], where they—in agreement with our finding—suggest that the vortex structures are suppressed by the spanwise oscillating Lorentz force.

Figure 22 presents the predicted turbulence production compared with DNS data [28]. The turbulence production near the lower wall is lower in the applied force case (Fig. 22a, c) than it is near the upper wall (Fig. 22b, d). There are two components in the turbulence production term, the shear stress and the mean velocity gradient. An illustration of these two components separately reveals that the largest reason for the low turbulence production is the Reynolds shear stresses, see Figs. 23 and 24.

The lower shear stress at the vicinity of the wall contributes to lower turbulence production for the applied force case compared to the no-force case (Fig. 24a, c), while it is vice-versa for the upper half of the channel (Fig. 24b, d). The location of maximum turbulence production exhibits a shift away from the wall for the applied force case compared to the no-force case (Fig. 22a, c), which corresponds to the locations of the maximum Reynolds shear stresses (Fig. 24a, c). In Figs. 23a and 24c it is shown that for both $Re_\tau = 180$ and $Re_\tau = 400$ cases the St_{opt} gives the largest contribution to the reduction in turbulent production. Although

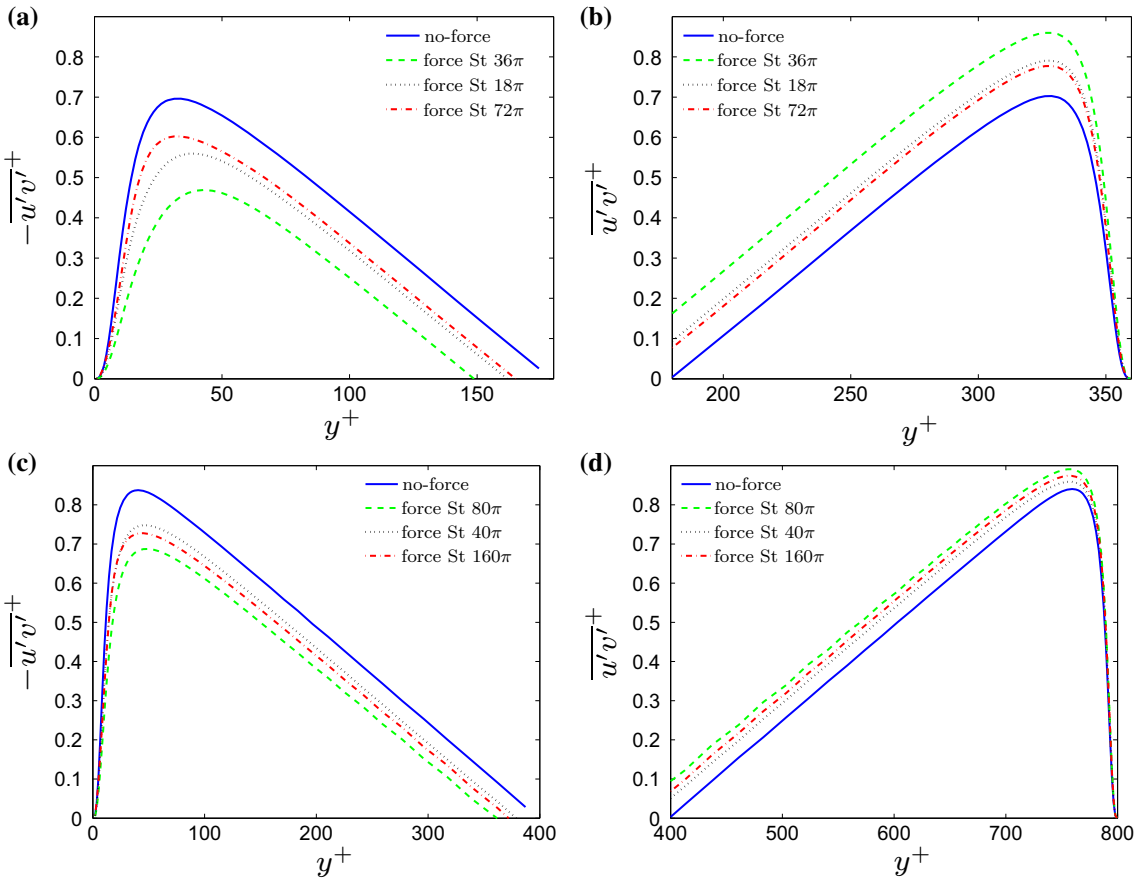

Fig. 24 Reynolds shear stress. **a** Lower wall, $Re_\tau = 180$, **b** upper wall, $Re_\tau = 180$, **c** lower wall, $Re_\tau = 400$, **d** upper wall, $Re_\tau = 400$

$St_{\text{opt}}/2$ gives the second largest contribution for $Re_\tau = 180$ case, it is $2St_{\text{opt}}$ for $Re_\tau = 400$ case. This is coherent with the results given by Berger et al. [5], where they reported that the required forcing increases with Reynolds number.

The drag reduction for the applied force case results in lower viscous effects near the lower wall and, in order to maintain the force balance in the streamwise direction, the drag force enhances at the upper wall. Thus, the upper wall statistics exhibits a corresponding enhancement to compensate for the lower wall reduction (Figs. 23b, d and 24b, d).

4 Conclusion

A DNS study of a fully developed turbulent channel flow was carried out by introducing a spanwise oscillating Lorentz force near the lower wall. We investigated the effect of the oscillating Lorentz force on wall structures. The results are examined in detail, not only for the applied force lower wall but also for the upper wall.

We found that in the applied force case the $R_{uu}(z)$ profile does not exhibit any minima for $y^+ < 20$ (Fig. 7a). The variation of the streamwise fluctuation velocities in the spanwise direction (Fig. 10) and the instantaneous velocity contours (Figs. 11, 12, 13, 14) lead us to suggest that the reason is more stable streaky structures in the applied force case.

We also observed that in the applied force case wall splattings are suppressed close to the wall ($y^+ \lesssim 20$) (Fig. 8a), which we suggest is related to smaller streamwise fluctuations near the wall (Figs. 4, 10a, b).

Although we observed for the applied force case a significant stabilization of the near-wall streaks below $y^+ \approx 20$ (Fig. 7a), the existence of streamwise vortices is obviously not affected by this stabilization (Fig. 9a). The streaks and the streamwise vortices are related to each other by the turbulence regeneration. It is shown by Jiménez and Pinelli [21] that the turbulence generation cycle is dependent on the area below $y^+ \approx 60$

and above $y^+ \approx 20$. In our study, we observed that, for $y^+ \gtrsim 30$, the fundamental structure of the streaks remains the same (Figs. 13, 14). It has been reported in the literature that spanwise Lorentz forcing causes an inclination of the streaky structures [9]. Our results support these findings (Figs. 11, 12), but we found that this inclination is not observable for $y^+ \gtrsim 30$ (Figs. 13, 14).

We observed that the region in which the sweeps dominate over the ejections extends further away from the wall in the applied force case (Fig. 15) than in the no-force case. In the fully turbulent region, it is found that the sweeps and ejections move away from the wall when forcing is applied (Fig. 16).

We showed that the $\partial v'/\partial z$ part of the streamwise vorticity, ω_x', is negligible compare to $\partial w'/\partial y$. Hence the latter component should be used to define the locations of the minima and maxima which also defines the radius of the mean Rankine vortex structures (Fig. 17). This suggests that the streamwise vorticity defines the radius of the mean Rankine vortex structures only in the wall-normal direction, not in the spanwise direction. The closer distance between the streamwise r.m.s. vorticity minima locations (Fig. 18) and unchanged $R_{vv}(z)$ profiles (Fig. 9a) in the applied force case lead us to claim that the spanwise oscillating Lorentz force creates an elliptic shape of the mean Rankine vortex structures (Fig. 19).

Finally, we analyzed the turbulence production and its components. We observed a lower turbulence production near the lower wall in the applied force case as compared with the no-force case, while the situation is reversed near the upper wall (Fig. 22). We observed that the main contribution to this difference in production is due to the magnitude of the Reynolds shear stress (Fig. 24) rather than the mean velocity gradient (Fig. 23).

Acknowledgements This study is financially supported by the Istanbul Technical University (ITU) and the Scientific and Technological Research Council of Turkey (TUBITAK). Computing resources used in this work were provided by the C3SE, the center for scientific and technical computing at Chalmers University of Technology. The first author thanks Lixia Qu for kind assistance.

References

1. Akoun, G., Yonnet, J.: 3D analytical calculation of the forces exerted between two cuboidal magnets. IEEE Trans. Magn. **20**(5), 1962–1964 (1984)
2. Albrecht, T., Metzkes, H., Grundmann, R., Mutschke, G., Gerbeth, G.: Tollmien-Schlichting wave damping by a streamwise oscillating Lorentz force. Magnetohydrodynamics **44**(3), 205–222 (2008)
3. Altintas, A., Davidson, L.: Direct numerical simulation of spanwise Lorentz force oscillations in turbulent channel flow at low Reynolds number. In: 14th European Turbulence Conference. Lyon, France (2013)
4. Bandyopadhyay, P.R., Castano, J.M.: Micro-tiles for electromagnetic turbulence control in saltwater-preliminary investigations. In: Symposium on Turbulence Modification and Drag Reduction, American Society of Mechanical Engineers Summer Meeting (1996)
5. Berger, T.W., Kim, J., Lee, C.: Turbulent boundary layer control utilizing the Lorentz force. Phys. Fluids **12**, 631–649 (2000)
6. Breuer, K.S., Park, J., Henoch, C.: Actuation and control of a turbulent channel flow using Lorentz forces. Phys. Fluids **16**(4), 897–907 (2004)
7. Choi, H., Moin, P., Kim, J.: Direct numerical simulation of turbulent flow over riblets. J. Fluid Mech. **255**, 503–539 (1993)
8. Choi, H., Moin, P., Kim, J.: Active turbulence control for drag reduction in wall-bounded flows. J. Fluid Mech. **261**, 75–110 (1994)
9. Crawford, C.H., Karniadakis, G.E.: Reynolds stress analysis of EMHD-controlled wall turbulence. Part I. Streamwise forcing. Phys. Fluids **9**, 788–806 (1997)
10. Davidson, L., Peng, S.H.: Hybrid LES-RANS: a one-equation SGS model combined with a $k-\omega$ model for predicting recirculating flows. Int. J. Numer. Fluids **43**, 1003–1018 (2001)
11. Du, Y., Karniadakis, G.E.: Suppressing wall turbulence by means of a transverse traveling wave. Science **288**, 1230–1234 (2000)
12. Du, Y., Symeonidis, V., Karniadakis, G.E.: Drag reduction in wall-bounded turbulence via a transverse travelling wave. J. Fluid Mech. **457**, 1–34 (2002)
13. Emvin, P., Davidson, L.: Development and implementation of a fast large eddy simulations method. Technical report, Dept. of Thermo and Fluid Dynamics, Chalmers University of Technology, Gothenburg (1997)
14. Gailitis, A.K., Lielausis, O.A.: On the possibility of drag reduction of a flat plate in an electrolyte. Appl. Magnetohydrodyn. Trudy Inst. Fisiky AN Latvia SSR **12**, 143–146 (1961)
15. Guo, H., Borodulin, V.I., Kachanov, Y.S., Pan, C., Wang, J.J., Lian, Q.X., Wang, S.F.: Nature of sweep and ejection events in transitional and turbulent boundary layers. J. Turbul. **11**, 1–51 (2010)
16. Hamilton, J.M., Kim, J., Waleffe, F.: Regeneration mechanism of near-wall turbulence structures. J. Fluid Mech. **287**, 317–348 (1995)

17. Henoch, C., Stace, J.: Experimental investigation of a salt water turbulent boundary layer modified by an applied streamwise magnetohydrodynamic body force. Phys. Fluids **7**, 1371–1383 (1995)
18. Huang, L.P., Fang, B.C., Mei, D.J.: Mechanism of drag reduction by spanwise oscillating Lorentz force in turbulent channel flow. Theor. Appl. Mech. Lett. **2**(1), 012005 (2012)
19. Iida, O., Nagano, Y.: The relaminarization mechanisms of turbulent channel flow at low Reynolds numbers. Flow Turbul. Combust. **60**, 193–213 (1998)
20. Jeong, J., Hussain, F., Schoppa, W., Kim, J.: Coherent structures near the wall in a turbulent channel flow. J. Fluid Mech. **332**, 185–214 (1997)
21. Jiménez, J., Pinelli, A.: The autonomous cycle of near-wall turbulence. J. Fluid Mech. **389**, 335–359 (1999)
22. Kim, J.: On the structure of wall-bounded turbulent flows. Phys. Fluids **26**, 2088–2097 (1983)
23. Kim, J.: Study of turbulence structure through numerical simulations: The perspective of drag reduction. Technical report, AGARD Report (1992)
24. Kim, J.: Physics and control of wall turbulence for drag reduction. Phil. Trans. R. Soc. A **369**, 1396–1411 (2011)
25. Kim, J., Moin, P., Moser, R.: Turbulence statistics in fully developed channel flow at low Reynolds number. J. Fluid Mech. **177**, 133–166 (1987)
26. Kline, S.J., Reynolds, W.C., Schraub, F.A., Runstadler, P.W.: The structure of turbulent boundary layers. J. Fluid Mech. **30**, 741–773 (1967)
27. Kravchenko, A.G., Choi, H., Moin, P.: On the relation of near-wall streamwise vortices to wall skin friction in turbulent boundary layers. Phys. Fluids A **5**, 3307–3309 (1993)
28. Moser, R.D., Kim, J., Mansour, N.N.: DNS of turbulent channel flow up to Re_τ=590. Phys. Fluids **11**, 943–945 (1999)
29. Moser, R.D., Moin, P.: Direct numerical simulation of curved turbulent channel flow. Technical Report 85974, NASA (1997)
30. Nilsson, H.: A parallel multiblock extension to the CALC-BFC code using pvm. Technical Report 9711, Department of Thermo and Fluid Dynamics, Chalmers University of Technology, Gothenburg (1984)
31. Nosenchuck, D.M., Brown, G.L.: Discrete spatial control of wall shear stress in a turbulent boundary layer. In: R.M.C. So, Speziale, C.G., Launder, B.E., (eds.) Near-Wall Turbulent Flows., pp. 313–343. Elsevier, New York (1993). Proceedings of an International Conference on Near-Wall Turbulent Flows held at Arizona State University, Tempe, AZ, March 15–17 (1993)
32. O'Sullivan, P.L., Biringen, S.: Direct numerical simulations of low reynolds number turbulent channel flow with EMHD control. Phys. Fluids **10**, 1169–1181 (1998)
33. Rhie, C.M., Chow, W.L.: Numerical study of the turbulent flow past an airfoil with trailing edge separation. AIAA J. **2**, 1525–1532 (1983)
34. Robinson, S.K.: Coherent motions in the turbulent boundary layer. Annu. Rev. Fluid Mech. **23**, 601–639 (1991)
35. Rossi, L., Thibault, J.P.: Investigation of wall normal electromagnetic actuator for seawater flow control. J. Turbul. **3**, 005 (2002)
36. Schoppa, W., Hussain, F.: Genesis and dynamics of coherent structures in near-wall turbulence. In: Panton, R. (ed.) Self-Sustaining Mechanisms of Wall Turbulence, p. 385. Computational Mechanics Publications, Southampton (1997)
37. Solbakken, S., Andersson, H.I.: On the drag reduction mechanism in a lubricated turbulent channel flow. Int. J. Heat Fluid Flow **25**, 618–624 (2004)
38. Xu, P., Choi, K.S.: Boundary layer control for drag reduction by Lorentz forcing. In: Morrison, J.E., Birch, D.M., Lavoie, P. (eds.) IUTAM Symposium on Flow Control and MEMS, pp. 259–265. Springer, Berlin (2008)